ABSTRACT

Diffuse optical tomography is an emerging technique for non-invasively measuring *in vivo* tissue optical properties. The next generation of DOT time domain imaging systems will allow researchers to create three-dimensional (3D) images of blood volume and oxygenation with unprecedented spatial resolution. We consider common semi-infinite and slab geometries, in the Born approximation to the diffusion equation. Current techniques for computing the 3D time-domain forward problem are computationally intensive: evaluating the required sensitivity matrix involves a numerical convolution in time. We present analytical results for this convolution, for both absorption and diffusion 3-point Green's functions. This accelerates calculation by up to two orders of magnitude, while improving accuracy.

Keywords: diffusive optical tomography, forward problem, time domain, Born approximation, sensitivity kernel

Fast computation of the time domain diffusion forward model for optical tomography in the Born approximation

Jonathan J. Stott

Quan Zhang

Athinoula A. Martinos Center for Biomedical Imaging,

Massachusetts General Hospital, Harvard Medical School,

Charlestown, MA 02129

Alex Barnett

Courant Institute of Mathematical Sciences,

New York University, NY 10012 David A. Boas

Athinoula A. Martinos Center for Biomedical Imaging,

Massachusetts General Hospital, Harvard Medical School,

Charlestown, MA 02129

1. INTRODUCTION

Diffuse optical tomography [DOT] is an emerging technique for non-invasive *in vivo* medical imaging.[1–3] Using optical fibers, near-infrared laser light is directed into biological tissue. As the light propagates through the tissue it is scattered many times and exits as a diffuse photon fluence. The intensity of the exiting photons is then measured using photo-detectors. Working in the diffusion approximation to the radiative transport equation,[4] the measured data can be inverted to provide information about the optical scattering and absorption of the region probed by the photons. If multiple overlapping measurements are available, tomographic reconstruction techniques can be used to produce three-dimensional images within a region of interest.[5,6]

By collecting data at multiple source wavelengths, the experimental optical absorption coefficients can be related back to the local concentration of oxy- and deoxy-hemoglobin (or, equivalently, to the total hemoglobin concentration and oxygen saturation). Knowledge of hemoglobin concentration has been used for functional imaging of human cerebral activity[7,2,8,9] and as a tool for locating breast cancer based on the associated tumor vasculature.[10,3,1,11]

Historically, many (but by no means all) of the original DOT imaging systems used either continuous-wave (CW) sources or sources amplitude modulated at radio frequencies (RF), typically in the range 70–300 MHz.[12–20] These systems were less complicated to design and usually gave better signal-to-noise performance than the available time domain imagers, in large part due to their smaller bandwidth requirements.[21] Time domain imagers, however, are

able to measure the complete temporal point spread function (TPSF) at each detector, due to each source, with a temporal resolution varying from less than 10 ps for streak cameras to 200 ps for gated image-intensified CCD detectors and photon counting systems.[22,23] To obtain the same information using a frequency domain imager would require multiple measurements at source modulation frequencies ranging from the tens of MHz up into the tens of GHz. It is this abundance of experimental information that makes time domain imagers an attractive imaging platform.[1,24–26]

Inverting data from a time domain imager, however, requires evaluating the forward problem,[27–29] by which we mean the TPSF appropriate to each source-detector measurement pair. When the scattering and absorption coefficients deviate sufficiently small amounts from a homogeneous medium, then a linear approximation can be used. In this case, evaluating the forward model amounts to finding the sensitivity (Frechét derivative) of the set of TPSF's with respect to infinitesimal changes in scattering and absorption at each point (voxel) in space. If the TPSF is considered as a discrete set of samples in time, then this derivative is expressed as a sensitivity matrix, or imaging kernel, $\mathcal{K}$. In simple geometries of interest, involving planar tissue-air interfaces, the method of images can be used. Many situations of medical relevance, such as functional brain imaging, can be well approximated by such geometries. Then the matrix elements of $\mathcal{K}$ are given in the form of analytically-known Green's functions for the homogeneous infinite medium. To find each matrix element, the Green's functions have to be summed over multiple images. However, because we are working in the time domain, for each matrix element an integration over intermediate times between the source pulse arrival time and the detection time is required. Because the ill-conditioned matrix $\mathcal{K}$ is subsequently inverted as part of the DOT inverse problem, its accuracy is important. One way to evaluate the sensitivity matrix $\mathcal{K}$ is to work in the frequency domain and Fourier transform to get the time domain result, but this requires computing a large number of frequencies. For example, our time domain imager uses a source laser with a pulse rate of 80 MHz (period $T = 12.5$ ns). To calculate the forward problem with a temporal resolution of $\Delta t = 100$ ps (on the same order of magnitude as our detector gate) therefore requires computing the forward problem at approximately $T/\Delta t = 125$ different frequencies.

The traditional alternative, namely computing $\mathcal{K}$ directly in the time domain via numerical integration over intermediate times, is also computationally demanding. As we show in Section 4.3, the rapid changes of the integrand over short timescales means that short time-steps, hence many function evaluations (of order 10^4) are required to perform numerical time integration to reasonable accuracy.

In this paper we present an exact analytical technique which treats the integral over intermediate times as a convolution and uses the Faltung (convolution) theorem. This results in formulas (27) and (30) for the time-domain 3-point Green's functions in a homogeneous infinite medium. These formulate involve no integration, and require very little computational effort beyond that of finding the usual (2-point) Green's function. The matrix elements of

$\mathcal{K}$ are then built by summing over the required image charges. In favorable experimental geometries, where few or no image charges are needed, we have thus reduced our calculation times more than 100-fold.

In Section 2 we outline the theory of the DOT forward problem in the Born approximation, and present Green's function results in an infinite medium, a semi-infinite medium, and an infinite slab. We define the sensitivity matrix and sketch its use in the DOT inverse problem. Section 4 presents our main analytical results, their use for calculation of the sensitivity matrix, and compares the speed of our approach with that of the traditional one in practical test cases. We discuss some further issues and conclude in Section 5. Appendix A contains a derivation of the frequency domain 2-point Green's function.

2. THEORETICAL BACKGROUND

Photon migration in a highly scattering and weakly absorbing medium is accurately described by the diffusion approximation to the radiative transport equation[4]

$$-\frac{1}{v}\nabla \cdot [D(\mathbf{r})\nabla\phi(\mathbf{r},t)] + \mu_a(\mathbf{r})\phi(\mathbf{r},t) + \frac{1}{v}\frac{\partial}{\partial t}\phi(\mathbf{r},t) = S_0(\mathbf{r},t) \qquad (1)$$

where ϕ is the fluence (proportional to the photon density), D is the diffusion coefficient, μ_a is the absorption coefficient (inverse absorption length), v is the local speed of light $v = c/n$, and S_0 is some distribution of isotropic point sources. The diffusion coefficient is normally written in terms of the reduced scattering coefficient μ_s' as follows[30,31]

$$D = \frac{v}{3\left(\mu_s' + \mu_a\right)} \approx \frac{v}{3\mu_s'}.$$

The signal measured at the detector is proportional to the fluence at the boundary.[27,32]

2.1. Two-point Green's function

In an optically-homogeneously medium, of general shape (geometry), the 2-point Green's function $G^{gen}(\mathbf{r}',\mathbf{r};t'-t)$ is defined by

$$-\frac{1}{v}\nabla' \cdot [D\nabla'G^{gen}] + \mu_a G^{gen} + \frac{1}{v}\frac{\partial}{\partial t'}G^{gen} = \delta(\mathbf{r}'-\mathbf{r})\delta(t'-t), \qquad (2)$$

and satisfies any boundary conditions (as a function of both $\mathbf{r}'$ and $\mathbf{r}$) that define the medium geometry. In other words, viewed as a function of primed coordinates, it gives the solution to (1) due to a unit-strength impulsive source S_0 which has location $\mathbf{r}$ and injection time t. In our notation we will use unprimed coordinates to denote a source injection (initial) location and time, and primed coordinates for a detection (final) location and time.

In an infinite optically-homogeneous medium, (2) takes the well-known analytic form[27,33]

$$G(\mathbf{r}'-\mathbf{r},t'-t) = \frac{\Theta(t'-t)}{[4\pi D(t'-t)]^{3/2}} \exp\left(-\frac{|\mathbf{r}'-\mathbf{r}|^2}{4D(t'-t)} - v\mu_a(t'-t)\right) \qquad (3)$$

where $\Theta(t)$ is the Heaviside step function

$$\Theta(t' - t) = \begin{cases} 1, & t' - t \geq 0 \\ 0 & \text{otherwise} \end{cases}$$

which serves to enforce causality (although the Green's function is still non-causal in a sense, since it allows signals to propagate faster than the speed of light). As is common in the literature, we will sometimes refer to (3) as the 'free-space' Green's function. Due to translational invariance of infinite space, the free-space Green's function G (unlike G^{gen}) depends only on the interval between the initial point (unprimed) and the final point (primed), hence we used the notation $G(\mathbf{r}', \mathbf{r}; t' - t) = G(\mathbf{r}' - \mathbf{r}, t' - t)$. Isotropy of space is responsible for the fact that G only depends on radial distance, for instance we can write $G(|\mathbf{r}' - \mathbf{r}|, t' - t)$; we will sometimes use this form for clarity. Due to invariance in time, both G and G^{gen} depend only on the time difference $(t' - t)$ in terms of which the TPSF is expressed.

2.2. Three-point Green's functions

Consider the homogeneous medium of general geometry. We now optically perturb the medium by $\delta\mu_a(\mathbf{r}'')$ in absorption coefficient and $\delta D(\mathbf{r}'')$ in diffusion coefficient. These are arbitrary functions of a spatial coordinate $\mathbf{r}''$. (They are assumed constant in time on typical photon transit timescales). We use $\phi^{meas}(\mathbf{r}', \mathbf{r}; t' - t)$ to denote the resulting solution to (1), written as a function of primed coordinates, due to the unit-strength impulsive source at location $\mathbf{r}$ and release time t. In the first-order Born approximation, ϕ^{meas} is written as a sum of the incident fluence ϕ^{inc} due to the homogeneous medium, and the fluence ϕ^{sc} scattered off of the various inhomogeneities in the volume,

$$\phi^{meas}(\mathbf{r}', \mathbf{r}; t' - t) = \phi^{inc}(\mathbf{r}', \mathbf{r}; t' - t) + \phi^{sc}(\mathbf{r}', \mathbf{r}; t' - t). \tag{4}$$

The first-order Born approximation is that ϕ^{sc} is a linear functional of $\delta\mu_a(\mathbf{r}'')$ and $\delta D(\mathbf{r}'')$. This is exact in the limit that the optical perturbations become infinitesimally small. For larger perturbations, this becomes the first term in a Dyson series.[34]

In a general geometry we have simply

$$\phi^{inc}(\mathbf{r}', \mathbf{r}; t' - t) = G^{gen}(\mathbf{r}', \mathbf{r}; t' - t). \tag{5}$$

The scattered fluence can be written as a volume integral of the perturbation,

$$\begin{aligned} \phi^{sc}(\mathbf{r}', \mathbf{r}; t, t') &= \int_V d^3\mathbf{r}'' \tilde{K}_a^{gen}(\mathbf{r}', \mathbf{r}'', \mathbf{r}; t' - t)\delta\mu_a(\mathbf{r}'') \\ &+ \int_V d^3\mathbf{r}'' \tilde{K}_d^{gen}(\mathbf{r}', \mathbf{r}'', \mathbf{r}; t' - t)\delta D(\mathbf{r}''). \end{aligned} \tag{6}$$

The time-integrated 3-point Green's functions, or imaging kernels, $\tilde{K}_a^{gen}$ and $\tilde{K}_d^{gen}$ correspond to sensitivity to absorption and diffusion coefficient changes respectively. Due to the general geometry, they are functions of the three locations $\mathbf{r}', \mathbf{r}$, and $\mathbf{r}''$, and of the time-difference $(t' - t)$.

The time-integration in question is over t'', the time of the 'scattering interaction event', that is

$$\tilde{K}_a^{gen}(\mathbf{r}',\mathbf{r}'',\mathbf{r};t'-t) = \int_t^{t'} dt'' K_a^{gen}(\mathbf{r}',\mathbf{r}'',\mathbf{r};t'-t'',t''-t),$$

$$\tilde{K}_d^{gen}(\mathbf{r}',\mathbf{r}'',\mathbf{r};t'-t) = \int_t^{t'} dt'' K_d^{gen}(\mathbf{r}',\mathbf{r}'',\mathbf{r};t'-t'',t''-t). \tag{7}$$

Our goal in this paper is evaluation of these time-integrations: we will be able to perform them analytically in certain geometries.

The kernels K_a and K_d are well-known and are given in terms of the 2-point Green's functions for the geometry in question;[35,5,30] we give the final results. The absorption kernel is

$$K_a^{gen}(\mathbf{r}',\mathbf{r}'',\mathbf{r};t'-t'',t''-t) = -G^{gen}(\mathbf{r}',\mathbf{r}'';t'-t'')\,G^{gen}(\mathbf{r}'',\mathbf{r};t''-t). \tag{8}$$

The diffusion kernel is

$$K_d^{gen}(\mathbf{r}',\mathbf{r}'',\mathbf{r};t'-t'',t''-t) = \frac{1}{v}\nabla' G^{gen}(\mathbf{r}',\mathbf{r}'';t'-t'')\cdot\nabla'' G^{gen}(\mathbf{r}'',\mathbf{r};t''-t). \tag{9}$$

where ∇' is the gradient with respect to the spatial argument $\mathbf{r}'$ and ∇'' is the gradient with respect to $\mathbf{r}''$.

Specializing to the infinite medium case, ϕ^{inc} is given by (5) with the substitution of G for G^{gen}. As special cases of (8) and (9), the free-space absorption kernel is

$$K_a(\mathbf{r}'-\mathbf{r}'',\mathbf{r}''-\mathbf{r};t'-t'',t''-t) = -G(\mathbf{r}'-\mathbf{r}'',t'-t'')\,G(\mathbf{r}''-\mathbf{r},t''-t), \tag{10}$$

and the free-space diffusion kernel is

$$K_d(\mathbf{r}'-\mathbf{r}'',\mathbf{r}''-\mathbf{r};t'-t'',t''-t) = \frac{1}{v}\nabla G(\mathbf{r}'-\mathbf{r}'',t'-t'')\cdot\nabla G(\mathbf{r}''-\mathbf{r},t''-t), \tag{11}$$

where ∇ is the gradient vector with respect to the spatial argument.

2.3. Semi-infinite and slab geometries

Two common analytically-tractable geometries of experimental relevance are the semi-infinite geometry and the infinite slab geometry (Figure 1b,c). Both of these can be solved using the method of images.[36] The air-tissue interface(s) are assumed to be parallel to the xy plane: at $z = 0$ for the semi-infinite case, and with a second interface at $z = L$ for the slab (where L is the thickness of the slab). A Dirichlet boundary condition $\phi(z) = 0$ is satisfied at some distance z_b outside each air-tissue interface. This is known as the extrapolated boundary condition.[32,27] The exact value of z_b is calculated from the Fresnel reflection coefficients;[32] typically $z_b \approx 1.96/\mu_s'$ for tissue of refractive index $n \approx 1.4$. In non-invasive imaging, source fibers terminate at the air-tissue interface. These sources are normally modeled by replacing the fiber (which assuming a low numerical aperture creates approximately an

exponentially-decaying line source) with a uniformly radiating point source located one reduced scattering length inside the medium.[27]

The method of images allows us to write for the semi-infinite geometry

$$G^{semi}(\mathbf{r}', \mathbf{r}; t' - t) = G(\mathbf{r}' - \mathbf{r}_0; t' - t) - G(\mathbf{r}' - \mathbf{r}_1; t' - t) \tag{12}$$

where $\mathbf{r}_0 = \mathbf{r}$ and its image $\mathbf{r}_1$ is generated from $\mathbf{r}$ by subtracting its z-coordinate from z_b (see Figure 1b). Here the total number of images is $I = 2$. For the infinite slab geometry

$$G^{slab}(\mathbf{r}', \mathbf{r}; t' - t) = \sum_{i=-(I-1)/2}^{(I-1)/2} (-1)^i G(\mathbf{r}' - \mathbf{r}_i; t' - t), \tag{13}$$

where I is the (odd) total number of charges summed, and the exact answer is reached in the limit $I \to \infty$. The locations $\mathbf{r}_i$ are given by the images of $\mathbf{r}$ due to multiple reflections in the extrapolated Dirichlet planes (see Figure 1c). In practice, though, the sum can be truncated to a modest I with high accuracy.[27,32] The number is modest due to the fact that the Gaussian form (3) has exponential tails in space. An estimate for I, given a relative truncation error ϵ, is[37]

$$I \approx \frac{4}{L} \sqrt{D T_{\max} \log(1/\epsilon)},$$

where $T_{\max}$ is the largest TPSF time $(t' - t)$ of interest (typically several ns) and L is the thickness of the slab. We find in typical biomedical applications, given $\epsilon \sim 10^{-6}$, that I rarely exceeds 10.

For the semi-infinite medium, substituting (12) into (8), using the spatial inversion symmetry of G, and regrouping via (10) gives

$$
\begin{aligned}
K_a^{semi}&(\mathbf{r}', \mathbf{r}'', \mathbf{r}; t' - t'', t'' - t) \\
&= K_a(\mathbf{r}'_0 - \mathbf{r}'', \mathbf{r}'' - \mathbf{r}_0; t' - t'', t'' - t) - K_a(\mathbf{r}'_1 - \mathbf{r}'', \mathbf{r}'' - \mathbf{r}_0; t' - t'', t'' - t) \\
&\quad - K_a(\mathbf{r}'_0 - \mathbf{r}'', \mathbf{r}'' - \mathbf{r}_1; t' - t'', t'' - t) + K_a(\mathbf{r}'_1 - \mathbf{r}'', \mathbf{r}'' - \mathbf{r}_1; t' - t'', t'' - t).
\end{aligned}
\tag{14}
$$

The expression for K_d^{semi} is of identical form (replacing a by s).

For the slab, substituting (13) in a similar fashion gives

$$K_a^{slab}(\mathbf{r}', \mathbf{r}'', \mathbf{r}; t' - t'', t'' - t) = \sum_{i=-(I-1)/2}^{(I-1)/2} \sum_{j=-(I-1)/2}^{(I-1)/2} (-1)^{i+j} K_a(\mathbf{r}'_i - \mathbf{r}'', \mathbf{r}'' - \mathbf{r}_j; t' - t'', t'' - t). \tag{15}$$

Again the expression for K_d^{slab} is of identical form.

Writing the 3-point Green's functions in the semi-infinite and slab geometries in terms of their free-space counterparts results in a double sum over image charges (one sum for each Green's function). Figure 1 shows these geometries, and arrangements of image charges that are required to compute the 3-point Green's functions. Note

that the choice to sum over source and detector images was arbitrary: it is equally-well possible to represent the 2-point Green's functions using sums over $\mathbf{r}''$, in which case the 3-point result will be a double sum over images of $\mathbf{r}''$. The requirement of a double sum cannot be changed.

2.4. Sensitivity matrix and the DOT linear inverse problem

A DOT system with a number S of sources, a number D of detectors, and a number M of time samples of the TPSF, produces a complete measurement vector $\mathbf{y}$ of dimension $\mathcal{M} = SDM$, Each component $m = 1, 2, \ldots \mathcal{M}$ has associated with it a source location $\mathbf{R}_m$, a detector location $\mathbf{R}'_m$, and a time-of-flight $T_m = t' - t$. The measurement vector is thus defined by

$$y_m = \phi^{meas}(\mathbf{R}'_m, \mathbf{R}_m; T_m). \tag{16}$$

We assume N voxels in the imaging volume, each with an unknown $\delta\mu_a$ and δD, thus there are $\mathcal{N} = 2N$ degrees of freedom in the inverse problem. We call this unknown vector of optical coefficient perturbations $\mathbf{x}$. Each component $n = 1, 2, \ldots \mathcal{N}$ has associated with it a centroid location of a voxel, $\mathbf{R}''_n$, and a label $l_n = \{a, d\}$ describing whether the degree of freedom is an absorption or diffusion perturbation.

The (rectangular $\mathcal{M}$ by $\mathcal{N}$) sensitivity matrix $\mathcal{K}$ is then defined by

$$\mathcal{K}_{mn} \equiv \frac{\partial y_m}{\partial x_n} = \tilde{K}_{l_n}^{gen}(\mathbf{R}'_m, \mathbf{R}''_n, \mathbf{R}_m; T_m), \tag{17}$$

where the second equality results from (6) and (4) substituted into (16).

The utility of $\mathcal{K}$ for time-resolved DOT is as follows. Given a known perturbation $\mathbf{x}$, the corresponding fluence $\mathbf{y}$, in the linear approximation, would be given by

$$\mathbf{y} = \mathbf{y}^{(0)} + \mathcal{K}\mathbf{x}, \tag{18}$$

where the unperturbed measurements are $\mathbf{y}_m^{(0)} = \phi^{inc}(\mathbf{R}'_m, \mathbf{R}_m; T_m)$. Given a real-world measurement vector $\mathbf{y}$, this linear relation can be inverted to give the optical perturbations

$$\mathbf{x} = \mathcal{K}^{-1}(\mathbf{y} - \mathbf{y}^{(0)}). \tag{19}$$

Generally K is ill-conditioned or singular, so in practice $\mathcal{K}^{-1}$ must be replaced by a regularized pseudo-inverse $\mathcal{K}^+$ for actual calculations.[30] The reference signal vector $\mathbf{y}^{(0)}$ can be either calculated or measured from a homogeneous phantom.

3. ANALYTIC FORM FOR FREE-SPACE TIME-INTEGRATED KERNELS

We now present our main result: the free-space equivalents of (7) can be found analytically. We will use the abbreviations $p \equiv |\mathbf{p}|$ and $q \equiv |\mathbf{q}|$, with

$$\mathbf{p} \equiv \mathbf{r}'' - \mathbf{r}, \qquad\qquad \mathbf{q} \equiv \mathbf{r}' - \mathbf{r}''. \tag{20}$$

The desired kernels are the time-integrals of (10) and (11), in our new notation,

$$
\begin{aligned}
\tilde{K}_a(\mathbf{q}, \mathbf{p}; t' - t) &= \int_t^{t'} dt'' K_a(\mathbf{q}, \mathbf{p}; t' - t'', t'' - t), \\
\tilde{K}_d(\mathbf{q}, \mathbf{p}; t' - t) &= \int_t^{t'} dt'' K_d(\mathbf{q}, \mathbf{p}; t' - t'', t'' - t).
\end{aligned}
\tag{21}
$$

As a preliminary we derive the free-space frequency domain 2-point Green's function $G(\mathbf{r}' - \mathbf{r}; \omega)$, by substituting its inverse Fourier transform

$$
G(\mathbf{r}' - \mathbf{r}, t' - t) = \int_{-\infty}^{\infty} \frac{d\omega}{2\pi} \exp\left(-i\omega(t' - t)\right) G(\mathbf{r}' - \mathbf{r}, \omega)
\tag{22}
$$

into the free-space version of (2). This gives

$$
G(\mathbf{r}' - \mathbf{r}; \omega) = \frac{\exp\left(-k(\omega)\left|\mathbf{r}' - \mathbf{r}\right|\right)}{4\pi D \left|\mathbf{r}' - \mathbf{r}\right|}
\tag{23}
$$

where the complex spatial decay constant obeys

$$
k(\omega)^2 = \frac{v\mu_a - i\omega}{D}.
$$

An alternative derivation is to Fourier transform the free-space time domain Green's function (3) directly (Appendix A).

3.1. Absorption kernel

First we tackle the absorption kernel. Substitution of (10) into (21), and writing in terms of scalars q, p, gives

$$
\begin{aligned}
\tilde{K}_a(\mathbf{q}, \mathbf{p}, t' - t) &= -\int_t^{t'} dt'' G(q, t' - t'') G(p, t'' - t) \\
&= -\int_t^{t'} dt'' \int_{-\infty}^{\infty} \frac{d\omega'}{2\pi} \int_{-\infty}^{\infty} \frac{d\omega}{2\pi} \exp\left(-i\omega'(t' - t'')\right) G(q, \omega') \exp\left(-i\omega(t'' - t)\right) G(p, \omega),
\end{aligned}
\tag{24}
$$

where in the latter step we substituted (22). Due to the Heaviside step function in the time domain Green's function the limits of integration in dt'' can be changed from $[t, t']$ to $[-\infty, \infty]$ since the integrand is everywhere zero except for $t \le t'' \le t'$. The integral over t'' now can be evaluated to yield the Dirac delta function $\delta(\omega - \omega')$, making the integral over ω' trivial. These steps are familiar from the standard proof of the convolution theorem. What we're left with is

$$
\tilde{K}_a(\mathbf{q}, \mathbf{p}; t' - t) = \int_{-\infty}^{\infty} \frac{d\omega}{2\pi} \exp\left(-i\omega(t' - t)\right) \frac{\exp\left(-k(\omega)p\right)}{4\pi Dp} \frac{\exp\left(-k(\omega)q\right)}{4\pi Dq}.
\tag{25}
$$

Remarkably, since the two ω's, and hence the two $k(\omega)$'s, are now identical, when we combine the exponents, the result has the functional form of a *single* frequency domain Green's function with a modified radial distance, $G(q + p, \omega)$, multiplied by a geometrical constant:

$$
\tilde{K}_a(\mathbf{q}, \mathbf{p}; t' - t) = \frac{q + p}{4\pi Dqp} \int_{-\infty}^{\infty} \frac{d\omega}{2\pi} \exp\left(-i\omega(t' - t)\right) \frac{\exp\left[-k(\omega)(q + p)\right]}{4\pi D(q + p)}.
\tag{26}
$$

It is this feature which allows a simple inverse Fourier transform back to the time domain. To make this explicit, by comparing the above to (23) and (22) we can write

$$\tilde{K}_a(\mathbf{q}, \mathbf{p}; t' - t) = \frac{1}{4\pi D} \left(\frac{1}{q} + \frac{1}{p} \right) G(q + p, t' - t), \tag{27}$$

completing our derivation.

3.2. Diffusion kernel

Now we tackle the diffusion kernel. Substitution of (11) into (21), and then using (22) gives

$$\tilde{K}_d(\mathbf{q}, \mathbf{p}; t' - t) = \frac{1}{v} \int_t^{t'} dt'' \, \nabla G(\mathbf{q}, t' - t'') \cdot \nabla G(\mathbf{p}, t'' - t)$$

$$= \frac{1}{v} \int_t^{t'} dt'' \int_{-\infty}^{\infty} \frac{d\omega'}{2\pi} \int_{-\infty}^{\infty} \frac{d\omega}{2\pi} \exp\left(-i\omega'(t' - t'') \right) \exp\left(-i\omega(t'' - t) \right) \nabla G(\mathbf{q}, \omega') \cdot \nabla G(\mathbf{p}, \omega).$$

Since the integrals are over time and frequency and the derivatives are in space, they commute and we can exchange the order of operations. Looking at (24), we can recognize the expression inside the integral is the same as the one for $\tilde{K}_a$, allowing us to write

$$\tilde{K}_d(\mathbf{q}, \mathbf{p}; t' - t) = -\frac{1}{v} \left(\nabla_{\mathbf{q}} \cdot \nabla_{\mathbf{p}} \right) \tilde{K}_a(\mathbf{q}, \mathbf{p}; t' - t). \tag{28}$$

Note that for the purposes of this derivation, $\mathbf{q}$ and $\mathbf{p}$ are independent variables, so the order of derivatives is immaterial. Because each 2-point free-space Green's function is a function only of scalar distance, we can make the substitutions,

$$\nabla_{\mathbf{q}} \to \hat{\mathbf{q}} \frac{\partial}{\partial q}, \qquad\qquad \nabla_{\mathbf{p}} \to \hat{\mathbf{p}} \frac{\partial}{\partial p}, \tag{29}$$

where the unit vectors are $\hat{\mathbf{q}} \equiv \mathbf{q}/q$ and $\hat{\mathbf{p}} \equiv \mathbf{p}/p$. We also substitute our analytic absorption kernel (27) to give,

$$\tilde{K}_d(\mathbf{q}, \mathbf{p}; t' - t) = -\frac{\hat{\mathbf{q}} \cdot \hat{\mathbf{p}}}{4\pi D v} \frac{\partial^2}{\partial q \partial p} \left[\left(\frac{1}{q} + \frac{1}{p} \right) G(q + p, t' - t) \right]$$

Finally the spatial derivatives can be taken using the form (3) of the free-space time domain 2-point Green's function, to give

$$\tilde{K}_d(\mathbf{q}, \mathbf{p}; t' - t) = \frac{\hat{\mathbf{q}} \cdot \hat{\mathbf{p}}}{8\pi D^2 v(t' - t)} \left(\frac{1}{q} + \frac{1}{p} \right) \left[1 - \frac{(q + p)^2}{2D(t' - t)} \right] G(q + p, t' - t), \tag{30}$$

completing our derivation. The ability to transform back to the time domain before the spatial derivatives are taken is the key to the simple analytic form.

4. EVALUATING THE FORWARD SENSITIVITY MATRIX

We see from (17) that computing each element of the dense matrix $\mathcal{K}$ requires evaluation of one of the time-integrated kernels (7), either the absorption or the diffusion kernel. The number of matrix elements required is $\mathcal{M}\mathcal{N} = 2SDMN$.

A small-scale DOT imaging application may have $S \sim 10$, $D \sim 10$, $M \sim 10$, $N \sim 10^3$, giving $\mathcal{MN} \sim 10^6$ matrix elements. The large-scale imaging applications we're interested in often have $S \sim 100$, $D \sim 100$, $M \sim 10$, and $N \sim 10^4$, giving $\mathcal{MN} > 10^9$. The notation of (7) implies a general geometry. Clearly for a particular choice of geometry, the kernels K_a and K_d appropriate for this geometry should be substituted as the integrands of (7).

4.1. Traditional numerical integration

When evaluating a time-integrated kernel (7) the traditional approach is to use numerical integration, requiring samples of the integrand at various t'' in the range t to t'. Each sample is found using the expression (8) or (9). Each geometry-dependent 2-point Green's function G^{gen} is calculated using (12) for the semi-infinite case, or (13) for the slab case. This choice is the most efficient since the results of two single sums over image charges are then multiplied together, and no double sum is necessary. If W is the number of time samples, and I the number of image charges, then the total number P of evaluations of the function G required to fill the $\mathcal{K}$ matrix is

$$P = 2\mathcal{MN}IW, \tag{31}$$

where the factor 2 came from the fact that two 2-point Green's functions are required. This determines our numerical effort. In practice, the evaluation of the exponential function dominates the computational cost. For a slab geometry with $I \sim 10$, $W \sim 100$, in the large-scale example above, this gives $P \sim 10^{12}$ evaluations, clearly a heavy computational load requiring hours to days of CPU time.

What determines the accuracy and number of samples W required for the numerical integration? Unfortunately the integrand can vary rapidly over timescales much shorter that the integration domain $t' - t$. Looking at (3) we can see that this occurs when distances involved in the 2-point Green's functions are small, for instance if a source and detector are physically close, or any optode and a voxel. Simple integration techniques like the trapezoid rule and Simpson's rule can be used,[38,39] but the integrals must be evaluated using small time steps ΔT if an accurate answer is to be obtained. We illustrate this with Figure 2, where we show convergence of the relative error obtained on a single matrix element, using the trapezoid rule. The expected $O(\Delta T^2)$ convergence is clear, and a small ΔT is needed to reach an acceptable error. Therefore a large W typically of the order of 10^3–10^4 is needed. In Figure 3 we show these relative errors as a function of time of flight T, for a single source, single detector, and a variety of voxel locations, at $\Delta T = 10\,\text{ps}$.

To improve the efficiency, Gaussian quadrature[38,39] or more sophisticated adaptive integration routines can be used. In Figure 4 we show the relative errors as a function of time, using the QUADPACK $qags$ routine,[40] (a Gauss-Kronrod 21-point integration routine combined with an adaptive subdivision algorithm) to perform the numerical integration. Errors are constitently lower than with our trapezoid example, and only $W = 10^2$–10^3 samples are

required. We believe that W cannot be reduced much below this lower bound of $W \approx 100$ without unacceptably sacrificing accuracy.

4.2. Fast analytic method

Our proposed new method is to use the double sum expressions for the 3-point Green's function in a given geometry, and substitute them into (7). To be explicit, for the semi-infinite case, the absorption kernel (14) (and the identical corresponding form for the diffusion kernel) should be used. For the infinite slab case, the absorption kernel (15) (and again the same corresponding form for the diffusion kernel) should be used. Since (7) is then in the form of a sum of free-space 3-point Green's functions, the integration over t'' can be performed analytically by substituting our results (27) or (30).

Thus the total required number of G evaluations is

$$P = \mathcal{M}\mathcal{N}I^2. \tag{32}$$

Comparing this to the traditional method, we see it is faster by a factor $2W/I$. In the next section we will see this speed gain in practice. It has the further advantage that no additional numerical errors are introduced, beyond those already present in the truncation of the image charge sum in slab geometries. As explained in Section 2.3, the image charge sum is exponentially convergent, hence the whole method can achieve guaranteed high accuracy for $\mathcal{K}$.

4.3. Results

We implemented both the traditional numerical integration method, an adaptive integration method, and the proposed analytic method as part of our existing Born approximation forward solver package. The results comparing the adaptive algorithm and our new analytical method are summarized in Table 1. The traditional numerical implementation (trapezoid rule with $\Delta T = 10\,\mathrm{ps}$) are not given in the table; typically they were an order of magnitude slower than the adaptive algorithm. We see that the improvements in speed in the infinite and semi-infinite geometries are dramatic, because I is 1 or 2 in these cases. Assuming that our program spends most of its time evaluating the Green's function, this means that the speed factor is essentially W, which is of order 10^2 in this case. The improvement in the infinite slab geometry is more modest, because the larger I means we start to pay the price of the I^2 terms in the double sum.

The veracity of the expressions we have derived has been checked numerically: the results obtained are indistinguishable (to within a precision of better than six decimal places) from those obtained by the traditional method when high-quality adaptive integration routines are used (Figure 4).

5. DISCUSSION AND CONCLUSIONS

The essence of our approach has been to sacrifice the single sums over image charges needed to compute G^{gen} in place of a double sum, and in exchange reap the benefit of performing the integration over intermediate times analytically. The double sum is unavoidable, because our analytic result applies to the free-space 3-point Green's function, and a double sum is needed to construct a 3-point Green's function in a certain geometry from free-space results using the method of images. Our method is applicable to any geometry for which the method of images is useful and any geometry where the convolution can be evaluated analytically.

It is possible that careful Gaussian quadrature or adaptive integration could reduce the typical W required in the traditional approach, rendering it competitive with our new proposal. However, our results in this paper indicate that unless a large number of image charges are needed, then the analytic results we present should always be preferable for their speed and accuracy. Because $\mathcal{K}$ is ill-conditioned, accuracy well below any measurement noise levels is crucial for the DOT inverse problem. Other than the exponentially-convergent image charge truncation, our method is exact.

In conclusion, we have presented a novel technique for computing the time domain forward DOT problem, in the Born approximation, in geometries that can be treated with the method of images. The computation of the sensitivity matrix is a time-consuming task when many voxels and measurements are involved. By applying the convolution theorem, we have found simple analytic expressions for the integral over intermediate times of the free-space 3-point Green's functions, in the case of both absorption- and diffusion-type perturbations. Sensitivity matrix elements are then built from these results using the method of images. The method is of order W/I times faster than the traditional numerical integration over W time-steps, when I images are involved. Furthermore, it is exact. Computation times in example tests are improved up to 100-fold, depending on the geometry of the problem (see Table 1). In DOT experiments where the use of analytically solvable geometries is justified (for example, many functional brain imaging experiments), these improvements are indisputably beneficial.

APPENDIX A. FREQUENCY DOMAIN GREEN'S FUNCTION

In this appendix, we would like to show that the Green's function for the frequency domain diffusion equation (23) is equal to the Fourier transform of the time domain Green's function (3). We begin by writing the Fourier transform of the time domain Green's function (3)

$$
\begin{aligned}
G(r, \omega) &= \int_{-\infty}^{\infty} dt \exp\left(i\omega t\right) G(r, t) \\
&= \int_{-\infty}^{\infty} dt \, \Theta(t) \exp\left(i\omega t\right) \frac{\exp\left(\frac{-r^2}{4Dt} - c\mu_a t\right)}{(r\pi Dt)^{3/2}}.
\end{aligned}
$$

Making the change of variables

$$s = (v\mu_a - i\omega)/D$$

$$t' - tu = Dt,$$

we end up with an expression that has the form of a Laplace transform

$$
\begin{aligned}
G(r,\omega) &= \int_0^\infty (r\pi\tau)^{-3/2} \exp\left(\frac{-r^2}{4\tau}\right) \exp\left(-s\tau\right) \frac{d\tau}{D} \\
&= \frac{1}{4\pi Dr} \int_0^\infty \exp\left(-s\tau\right) \left[r\left(2\sqrt{\pi\tau^3}\right)^{-1} \exp\left(\frac{-r^2}{4\tau}\right)\right] d\tau
\end{aligned}
\tag{33}
$$

Looking in a table of Laplace transforms,[41] we find

$$\mathcal{L}\left\{\frac{k}{2\sqrt{\pi t^3}} \exp\left(\frac{-k^2}{4t}\right)\right\} = \exp\left(-k\sqrt{s}\right)$$

and so taking the Laplace transform (33) leaves us with

$$G(r,\omega) = \frac{\exp\left(-\sqrt{s}r\right)}{4\pi Dr}.$$

What we previously called $k(\omega)$, however, is nothing more than $\sqrt{s} = \sqrt{(c\mu_a - i\omega)/D}$ so

$$G(r,\omega) = \frac{\exp\left(-k(\omega)r\right)}{4\pi Dr}$$

which is the Green's function (23) for the frequency domain diffusion equation. The derivation from frequency domain to time domain proceeds in the same way with the Heaviside step function $\Theta(t)$ implicit in the definition of the inverse Laplace transform.

ACKNOWLEDGMENTS

REFERENCES

1. D. Grosenick, H. Wabnitz, H. H. Rinneberg, K. T. Moesta, and P. M. Schlag, "Development of a time-domain optical mammograph and first *in vivo* applications," *Applied Optics* **38**(13), pp. 2927–2943, 1999.

2. S. Fantini, M. A. Franceschini, E. Gratton, D. Hueber, W. Rosenfeld, D. Maulik, P. G. Stubblefield, and M. R. Stankovic, "Non-invasive optical mapping of the piglet brain in real time," *Opt. Express* **4**(8), pp. 308–314, 1999.

3. T. O. McBride, B. W. Pogue, E. D. Gerety, S. B. Poplack, U. L. Osterberg, and K. D. Paulse, "Spectroscopic diffuse optical tomography for the quantitative assessment of hemoglobin concentration and oxygen saturation in breast tissue," *Applied Optics* **38**, pp. 5480–5490, 1999.

4. S. Chandrasekhar, *Radiative transfer*, Dover Publications, New York, 1960.

5. A. C. Kak and M. Slaney, *Principles of computerized tomographic imaging*, IEEE Press, New York, 1988.

6. A. Yodh and B. Chance, "Spectroscopy and imaging with diffusing light," *Phys. Today* **48**, pp. 34–40, 1995.

7. M. A. Franceschini, V. Toronov, M. E. Filiaci, E. Gratton, and S. Fantini, "On-line optical imaging of the human brain with 160-ms temporal resolution," *Opt. Express* **6**(3), pp. 49–57, 2000.

8. A. H. Hielscher, A. Y. Bluestone, C. H. Schmitz, R. L. Barbour, and G. S. Abdoulaev, "Volumetric imaging of hemodynamic effects in the human brain by three-dimensional diffuse optical tomography," in *Advances in Optical Imaging and Photon Migration*, OSA Biomedical Topical Meetings, pp. 310–312, April 2002.

9. J. P. Culver, T. Durduran, D. Furuya, C. Cheung, J. H. Greenberg, and A. G. Yodh, "Diffuse optical measurement of hemoglobin and cerebral blood flow in rat brain during hypercapnia, hypoxia, and cardiac arrest." accepted by Adv. Exp Biol.

10. B. Chance, "Near-infrared (nir) optical spectroscopy characterizes breast tissue hormonal and age status," *Acad. Radiol.* **8**, pp. 209–210, 2001.

11. A. E. Cerussi, A. J. Berger, F. Bevilacqua, N. Shah, D. Jakubowski, J. Butler, R. Holcombe, and B. Tromberg, "Sources of absorption and scattering contrast for near-infrared optical mammography," *Acad. Radiol.* **8**, pp. 211–218, 2001.

12. B. W. Pogue, M. Testorf, T. McBride, U. Österberg, and K. Paulsen, "Instrumentation and design of a frequency-domain diffuse optical tomography imager for breast cancer detection," *Opt. Express* **1**(13), pp. 391–403, 1997.

13. M. A. Franceschini, K. T. Moesta, S. Fantini, G. Gaida, E. Gratton, H. Jess, W. W. Mantulin, M. Seeber, P. M. Schlag, and M. Kaschke, "Frequency-domain techniques enhance optical mammography: Initial clinical results," *Proc. Nat. Acad. Sci.* **94**, pp. 6468–6473, 1997.

14. J. S. Reynolds, T. L. Troy, R. H. Mayer, A. B. Thompson, D. J. Waters, K. K. Cornell, P. W. Snyder, and E. M. Sevick-Muraca, "Imaging of spontaneous canine mammary tumors using fluorescent contrast agents," *Photochem. Photobiol.* **70**(1), pp. 87–94, 1999.

15. Y. Yao, Y. Wang, Y. Pei, W. Zhu, J. Hu, and R. L. Barbour, "Frequency domain optical tomography in human tissue," in *Experimental, Numerical Methods for Solving Ill-Posed Inverse Problems: Medical, Nonmedical Applications*, No. 2570 in SPIE, pp. 254–266, 1995.

16. A. M. Siegel, J. J. A. Marota, and D. A. Boas, "Design and evaluation of a continuous-wave diffuse optical tomography system," *Opt. Express* **4**(8), pp. 287–298, 1999.

17. C. H. Schmitz, H. L. Graber, H. Luo, I. Arif, J. Hira, Y. Pei, A. Bluestone, S. Zhong, R. Andronica, I. Soller, N. Ramirez, S.-L. S. Barbour, and R. L. Barbour, "Instrumentation and calibration protocol for imaging dynamic features in dense-scattering media by optical tomography," *Applied Optics* **39**, pp. 6466–6486, 2000.

18. H. L. Graber, J. Chang, and R. L. Barbour, "Imaging of multiple targets in dense scattering media," in *Experimental and Numerical Methods for Solving Ill-Posed Inverse Problems: Medical and Nonmedical Applications*, No. 2570 in SPIE, pp. 219–234, 1995.

19. J. C. Hebden, S. R. Arridge, and D. T. Delpy, "Optical imaging in medicine: I. experimental techniques," *Phys. Med. Biol.* **42**, pp. 825–840, 1997.

20. C. H. Schmitz, M. Löcker, J. M. Lasker, A. H. Hielscher, and R. L. Barbour, "Instrumentation for fast fucntional optical tomography," *Rev. Sci. Inst.* **73**(2), pp. 429–439, 2002.

21. B. Chance, M. Cope, E. Gratton, N. Ramanujam, and B. Tromberg, "Phase measurement of light absorption and scatter in human tissue," *Rev. Sci. Inst.* **68**(10), 1998.

22. F. E. W. Schmidt, M. E. Fry, E. M. C. Hillman, J. C. Hebden, and D. T. Delpy, "A 32-channel time-resolved instrument for medical optical tomography," *Rev. Sci. Inst.* **71**(1), pp. 256–265, 2000.

23. V. Ntziachristos, X. Ma, and B. Chance, "Time-correlated single photon counting imager for simultaneous magnetic resonance and near-infrared mammography," *Rev. Sci. Inst.* **69**(12), pp. 4221–4233, 1998.

24. R. Cubeddu, A. Pifferi, P. Taroni, A. Torricelli, and G. Valentini, "Time-resolved imaging on a realistic tissue phantom: μ_s' and μ_a images versus time-integrated images," *Applied Optics* **35**(22), pp. 4533–4540, 1996.

25. R. Cubeddu, A. Pifferi, P. Taroni, A. Torricelli, and G. Valentini, "Imaging with diffusing light: an experimental study of the effect of background optical properties," *Applied Optics* **37**(16), pp. 3564–3573, 1998.

26. E. M. C. Hillman, J. C. Hebden, M. Schweiger, H. Dehghani, F. E. W. Schmidt, D. T. Delpy, and S. R. Arridge, "Time resolved optical tomography of the human forearm," *Phys. Med. Biol.* **46**, pp. 1117–1130, 2001.

27. M. S. Patterson, B. Chance, and B. C. Wilson, "Time resolved reflectance and transmittance for the non-invasive measurement of tissue optical properties," *Applied Optics* **28**(12), pp. 2331–2336, 1989.

28. F. Gao, P. Poulet, and Y. Yamada, "Simultaneous mapping of absorption and scattering coefficients from a three-dimensional model of time-resolved optical tomography," *Applied Optics* **39**(31), pp. 5898–5910, 2000.

29. F. Gao, H. Zhao, and Y. Yamada, "Improvement of image quality in diffuse optical tomography by use of full time-resolved data," *Applied Optics* **41**(4), pp. 778–791, 2002.

30. S. R. Arridge, "Optical tomography in medical imaging," *Inverse Problems* **15**, pp. R41–R93, 1999.

31. T. Durduran, A. G. Yodh, B. Chance, and D. A. Boas, "Does the photon-diffusion coefficient depend on absorption?," *J. Opt. Soc. Am. A* **14**(12), pp. 3358–3365, 1997.

32. R. C. Haskell, L. O. Svaasand, T.-T. Tsay, T.-C. Feng, M. S. McAdams, and B. J. Tromberg, "Boundary conditions for the diffusion equation in radiative transport," *J. Opt. Soc. Am.* **11**(10), pp. 2727–2741, 1994.

33. R. B. Guenther and J. W. Lee, *Partial differential equations of mathematical physics and integral equations*, Prentice Hall, Englewood Cliffs, NJ, 1988.

34. M. C. W. van Rossum and T. M. Nieuwenhuizen, "Multiple scattering of classical waves: microscopy, mesoscopy, and diffusion," *Rev. Mod. Phys.* **71**(1), pp. 313–371, 1999.

35. M. A. O'Leary, *Imaging with diffuse photon density waves*. PhD thesis, University of Pennsylvania, Department of Physics, 1996.

36. J. D. Jackson, *Classical electrodynamics*, J. Wiley and Sons, New York, 1975.

37. A. Barnett in preparation.

38. G. H. Golub and J. M. Ortega, *Scientific computing and differential equations: an introduction to numerical methods*, Academic Press, Inc., San Diego, second ed., 1981.

39. R. L. Burden and J. D. Faires, *Numerical analysis*, PWS-KENT Publishing Company, Boston, fourth ed., 1989.

40. available on-line at 'http://www.netlib.org/'.

41. M. Abramowitz and I. A. Stegun, *Handbook of mathematical functions*, Dover Publications, Inc., New York, 1964.

Geometry	Analytic	Numeric	Ratio
Infinite	0.037 sec	4.58 sec	124:1
Semi-Infinite	0.104 sec	10.92 sec	105:1
Infinite Slab	2.065 sec	37.55 sec	18:1

Table 1. CPU time required to evaluate a forward sensitivity matrix $\mathcal{K}$ using our analytical formulation ("Analytic") compared with a direct numerical integration ("Numeric"). The numeric integration was performed using an adaptive integration algorithm; times for the trapezoid rule with $\Delta t = 10$ ps were roughly an order of magnitude larger. The ratio column gives the ratio of the two CPU times (i.e., the speed-up provided by our algorithm). For this test we used $S = 1$, $D = 4$, $M = 250$, $N = 5$. For slab geometries, the code chooses I automatically to satisfy an acceptable error requirement; typically $I \approx 6$. Similarly, W is typically in the range $W \approx 100$–200. The optical properties we used were $n = 1.4$, $\mu_s' = 8.0 \, \mathrm{cm}^{-1}$, $\mu_a = 0.05 \, \mathrm{cm}^{-1}$, and the thickness of the slab was $5 \, \mathrm{cm}$.
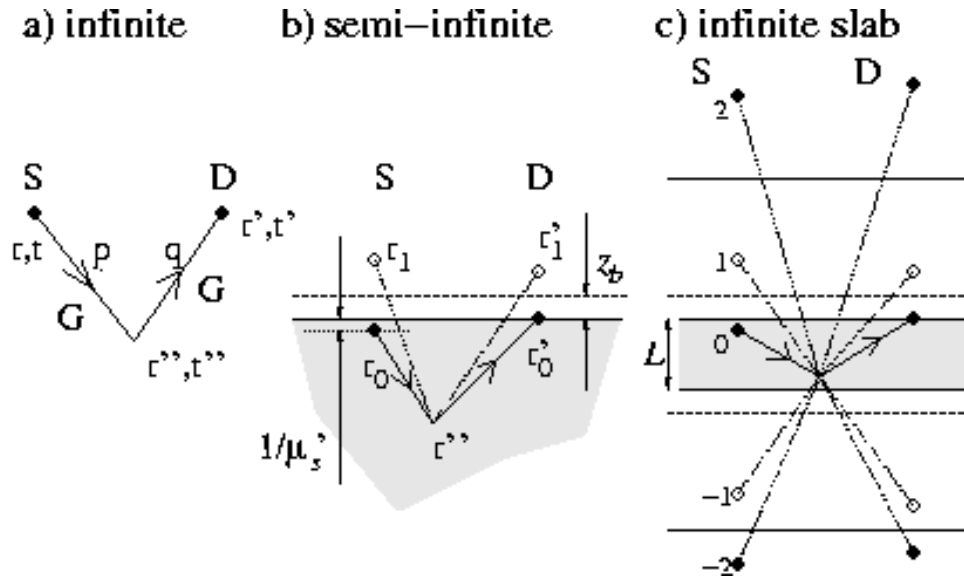
Figure 1. Diagrammatic representation of the 3-point Green's function in the three geometries of interest. The infinite medium case a) represents the free-space 3-point Green's function, composed of 2-point free-space Green's functions from $\mathbf{r}$ to $\mathbf{r}''$, and $\mathbf{r}''$ to $\mathbf{r}'$. Interaction with the inhomogeneity happens at $\mathbf{r}''$. In case b) each 2-point Green's function requires 2 terms (source S and detector D each require an image charge), giving a sum of 4 free-space 3-point functions. In case c) each 2-point Green's function has I terms (here $I = 5$), giving a sum of I^2 free-space 3-point functions. The dashed line shows the presence of an extrapolated boundary condition. Dash-dotted lines show its mirror images. A closed circle is a positive image charge, an open circle negative.
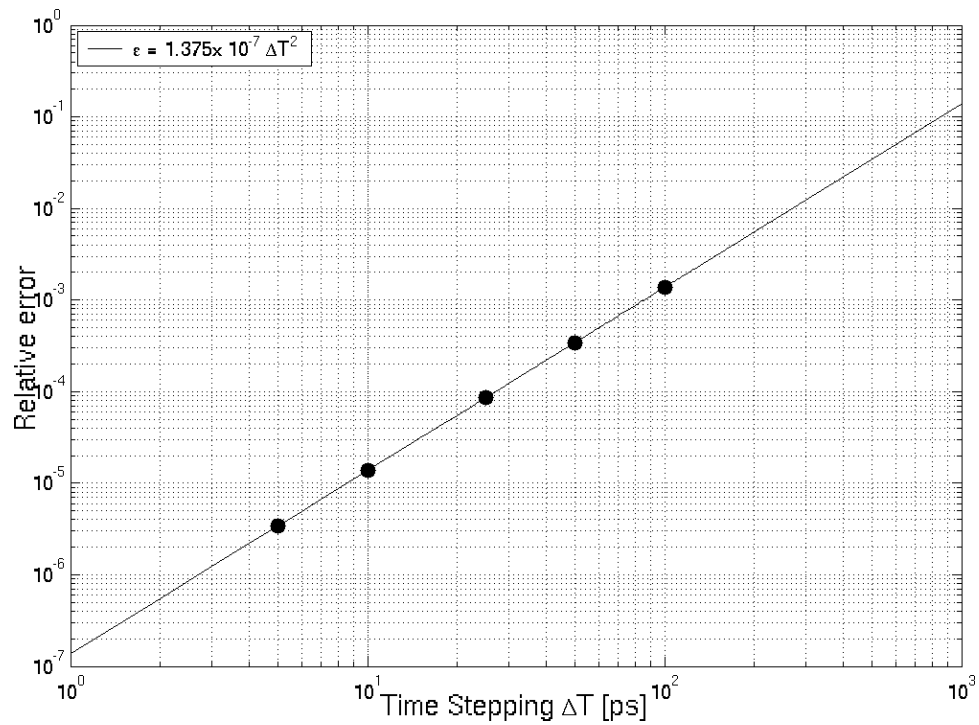
Figure 2. Error ϵ in the calculation of a representative element of the forward sensitivity matrix $\mathcal{K}$ as a function of the numerical time-integration step size ΔT. A simple trapezoidal rule is used. Circles mark the points at which the error was computed numerically, the solid line is a fit to the data. From the fit, we verified that the error is proportional to ΔT^2: $\epsilon = 1.375 \times 10^{-7} \Delta T^2$ where ΔT is specified in picoseconds.
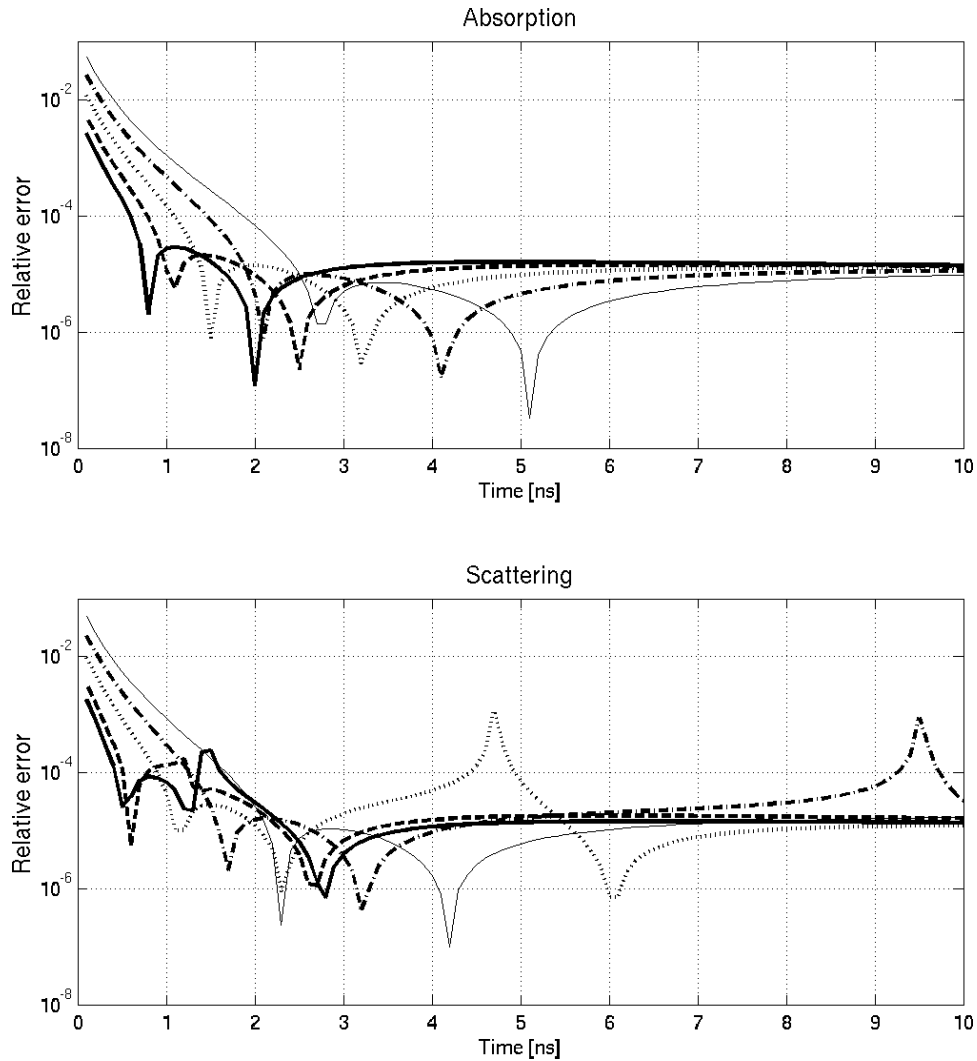
Figure 3. Magnitude of the relative difference between five sample TPSF's, when the time integrals for each time point are evaluated using trapezoid rule and an adaptive integration routine. The geometry was: one source at $(0,0,0)$, one detector at $(4,0,0)$, five voxels located between $(1.5,1.0,0.5)$ and $(1.5,1.0,4.5)$ in increments of 1 in a semi-infinite geometry (drawn as a solid line, dashed line, dotted line, dash-dotted line, and a fine solid line, respectively). All distance units are in cm. The time stepping used was $h = 10\,\text{ps}$. Deviations of order 1% occur at early times, falling to a slowly-varying magnitude at late times. The "spikes" visible throughout the plots are artifacts of the log-scale and occur whenever the relative error changes sign.
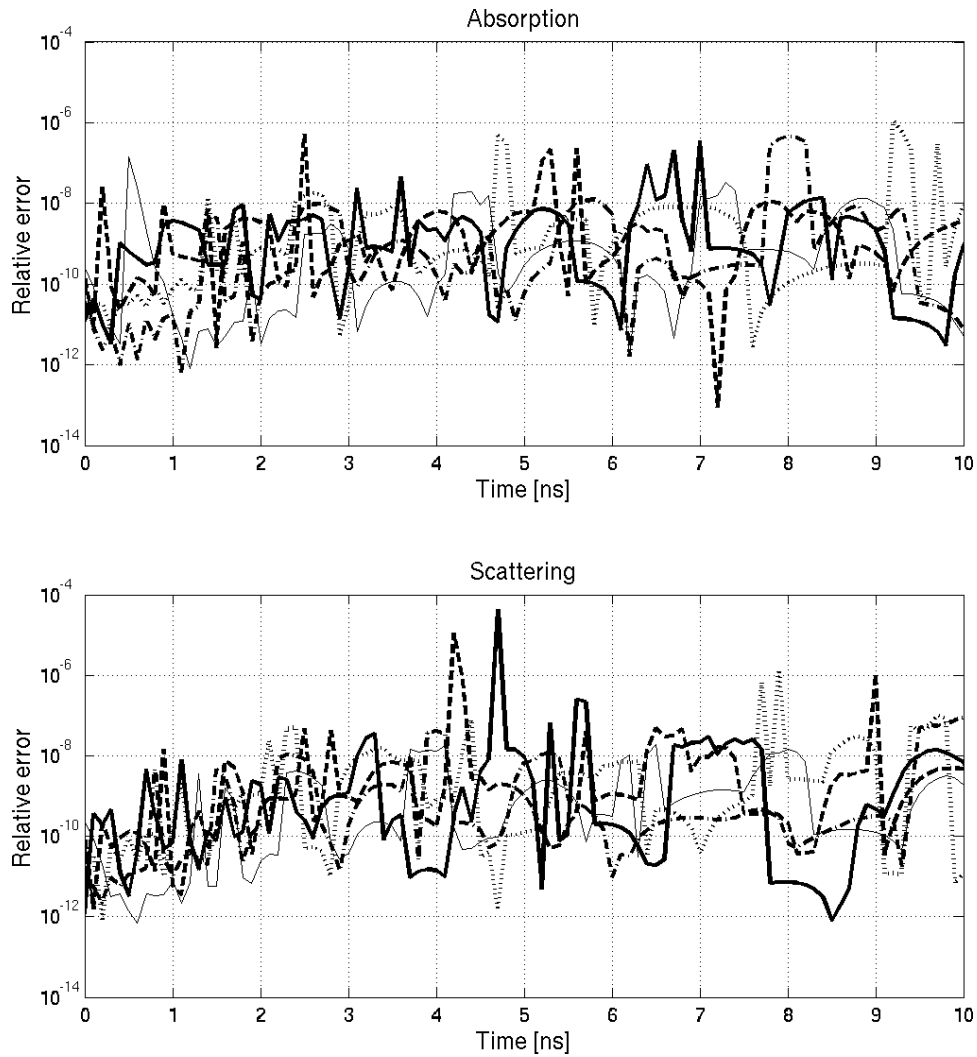
Figure 4. Magnitude of the relative difference between five sample TPSF's, when the time integrals for each time point are evaluated using an adaptive integration routine and our analytical expression. The accuracy of the adaptive algorithm can be controlled by setting an error bound. The relative error bound we used to generate this data was 10^{-4}. The geometry was the same as that of Figure 3. The different line styles also represent the same distances as in Figure 3.